Surface & Coatings Technology 485 (2024) 130867

Contents lists available at ScienceDirect

Surface & Coatings Technology

journal homepage: www.elsevier.com/locate/surfcoat

Full Length Article

How increasing cold spray coatings thickness affects their residual stress and properties

Rodolpho F. Vaz *, Andrea Garfias, Vicente Albaladejo, Javier Sanchez, Irene Garcia Cano

Thermal Spray Centre (CPT), Departament of Materials Science and Physical Chemistry, Universitat de Barcelona, Carrer Martí i Franquès 1, 08028 Barcelona, Spain

ARTICLE INFO

Keywords:
316 L
Cu
Ti
Cold spraying
Microstructure
Residual stress

ABSTRACT

Cold spray (CS) is a solid state deposition presented in the literature to produce coatings for various applications, e.g., corrosion-resistant 316L stainless steel, Ti light alloy parts repairing, and hydrophobic Cu coatings. CS sprays particles under high velocity, impacting onto a prepared surface or substrate, and the powders bond by a severe and fast plastic deformation, consolidating the coating layer by layer. The number of layers depends on the designed coating thickness since each powder and CS parameters results in a different layer thickness. This work evaluates three feedstock powders (Cu, Ti, and 316L) for CS processing, and the characteristics and properties of the CS-ed coatings, studying the effects of the thickness coatings on their microstructure, porosity, hardness, adhesion to the substrate, and residual stress generated. The images of microstructures were obtained by optical microscopy and SEM, and the near-to-surface residual stress was measured by X-ray diffraction (XRD). Increasing the coating thickness produced a substrate deformation due to the compressive residual stress dominating the coating, which is numerically obtained and proven by XRD. Besides that, increasing the coating thickness slight increased the deposition efficiency for Cu ant Ti, but went in the opposite way for 316L; reduced the coating adhesion to the substrate; and did not altered significantly the hardness.

1. Introduction

Cold spray (CS) is a solid-state deposition applied for many materials to make coatings or additive manufactured parts. Nowadays, the CS deposition of metals is more developed and industrially applied, while ceramic, composites, and polymeric CS-ed coatings have been studied at the academic level with promising results [1]. For CS processing, the sprayed particles remain in a solid-state during the deposition, impacting the substrate at supersonic speeds, deforming and anchoring or bonding by an intimate contact between the particles, which happens by the native surface oxides braking and removing at the impact, also called adiabatic shear instability (ASI) [2]. As consequences of ASI, jetting, mixing, local interface melting, and mechanical interlocking are also presented in the literature for CS-ed material consolidation [3,4]. CS prevents oxidizing and other thermal degradations of raw materials seen in thermal spraying processes, i.e., melting, solidification, and evaporation, which do not occur for CS [5–7], producing coatings from a few microns to millimetres scale thick.

The feedstocks for CS deposition are powders with specific characteristics to make feasible the coating consolidation. The chemical composition is not a limitation; however, regarding the mechanical properties, materials with high plasticity or ductility have presented better CS deposition efficiency, e.g., Cu, Al, or Ti alloys [8]. Spherical or irregular particles can be employed with similar results, reducing the CS deposition costs, because spherical powders are more expensive than irregular ones [9]. This last one can be applied to produce excellent coating properties, as seen in a comparison of microstructure, properties, and performance of CS-ed 316L coatings obtained with water and gas atomized particles [10]. The particle size distribution effects the particle velocity reached during the deposition, and a minimum velocity, critical velocity (v_{cr}), is presented in the literature for the material bonding by ASI [11,12]. For Cu, Ti, and 316L, v_{cr} is 570, 700, and 550 $m{\cdot}s^{-1}$, respectively [9]. The literature presents the v_{cr} of the particles dependent on their size, and smaller particles have much higher v_{cr} than the bigger ones [13,14]. The v_{cr} decreases sharply with the particle size increasing up to 50 μm; however, the effect of particle size is negligible beyond this particle size [11,13].

The literature presents many articles and book chapters discussing the microstructures and properties of CS-ed materials, optimization of CS parameters, hybrid processing, and post-treatments [9,15,16]. The

* Corresponding author.
E-mail address: rvaz@cptub.eu (R.F. Vaz).

https://doi.org/10.1016/j.surfcoat.2024.130867
Received 18 January 2024; Received in revised form 15 March 2024; Accepted 28 April 2024
Available online 29 April 2024

scholars have increased their interest in residual stress evolution on CS-ed coatings, and this work contributes to this theme by studying the effect of the CS-ed coating thickness on the material microstructure, properties, and residual stress of pure Cu, pure Ti, and 316L stainless steel. This is particularly interesting for industrial applications to limit the coating thickness feasible for each material, guaranteeing the coating performance under the working loading. Residual stress is the internal stress that remains locked within a material after manufacturing and without any external loads. The literature presents the residual stress classified into three types: macro-stresses, homogeneous over multiple grains; micro-stresses, over single grains; and micro-stresses in small portions of single grains [17]. For micro-stress, non-destructive X-ray diffraction (XRD) has been used for CS coatings, penetrating a few micrometers in the material, accrediting it just for superficial evaluation [18].

This work aims to compare the properties of CS Cu, Ti, and 316L coatings with single- and multi-layers, evidencing the effects of increasing the CS coating thickness on the microstructural characteristics, hardness, adhesion to the substrate, and residual stress.

2. Materials and methods

2.1. Feedstock powders

For the tests carried out in this work, three different commercial powders were used: gas-atomized pure Cu (Safina, Vestec, Czech Republic) and pure Ti (AP&C, Boisbriand, QC, Canada), and water-atomized 316L (Daye, Shijiazhuang, China). The powders chemical compositions were measured by inductively couple plasma (ICP) using an Optima ICP-OES 3200 RL (Perkin Elmer, Waltham, MA, USA) equipment. The elements below 0.1 wt% were not listed and were considered residual elements. The particle size distribution of feedstock powders was determined in triplicate by dry mode laser scattering (LS) technique using a LS13320 (Beckman Coulter, Brea, CA, USA) equipment, according to ASTM B822-02 [19] standard, and the particles shape were observed by scanning electron microscopy (SEM) in a Pro Desktop SEM (Thermo Fisher Phenom, Eindhoven, The Netherlands) equipment. To obtain the materials lattice structures free-stress condition, the powders were characterized in an X'Pert PRO MPD XRD (PANalytical, Malvern, United Kingdom) equipment with radiation of Cu Kα ($\lambda = 1.5418$ Å) from 5 to 120° 2θ with a 0.017° step, measuring 80 s per step, work power 45 kV and 40 mA. The crystal structures of the samples were identified using the PANalytical X'Pert Highscore Plus v.2.0a software utilizing the International Centre for Diffraction Data (ICDD) powder diffraction file (PDF) database for reference.

2.2. Cold spray deposition

All the feedstock powders were deposited onto flat low-carbon steel substrates ($225 \times 25 \times 2$ mm^3) previously grit-blasted with new alumina for surface cleaning and activation [20], reaching roughness greater than Ra 7 μm and Ry 40 μm. CS employed a high-pressure Kinetiks 4000 (Cold Gas Technology, Haun, Germany) equipment to produce the coatings. The CS parameters are presented in Table 1. The robot followed a kind of zigzag spraying strategy, presented schematically in Fig. 1(b) and also called traditional [21]. The parameters were a linear velocity of 500 mm·s^{-1}, and a step of 1 mm. A layer was considered after the robot recovered all the substrate surface area, and a different number of layers were considered for this study to reach 1 mm thick coatings. The parameters were selected based on the maximum deposition efficiency (DE) previously studied by the research group.

Table 1
CS spraying parameters.

Powder	Parameter				
	Gas type	Gas pressure [MPa]	Gas temperature [°C]	Powder feeding [g·s^{-1}]	Standoff distance mm]
Cu	N_2	3.0	400	0.75	40
Ti		4.0	700	0.74	40
316L		4.0	800	0.41	30

2.3. Characterization and mechanical properties

The DE is the fed powders/coating mass ratio, measured in a scale Mettler AE100 scale (Columbus, OH, USA) for the CS-ed samples. The metallographic preparation of CS-ed coatings followed the ASTM E1920-03 [22] and ASTM E3-01 [23] standards. A DMI5000M (Leica, Wetzlar, Germany) microscope was used for the optical microscopy (OM) and coating thickness measurement, following the ASTM B487-85 [24] standard, as an average of ten thickness values. To reveal the interparticular regions, Kroll's and aqua regia reagents were applied for Ti and 316L coatings, respectively, whereas Cu coatings revealed these boundaries during the polishing preparation step. Coatings' images were obtained by OM and SEM, and the coatings porosity was evaluated with ImageJ software on OM images, according to ASTM E2109-01 [25] standard. The flattening ratio was evaluated by comparing the shape of the coating's deformed particles with the spherical feedstock powder. The flattening ratio value was the mean of ten ratios measuring between the crossed longest and shortest particle dimensions. An HMV (Shimadzu, Tokyo, Japan) equipment was used for microhardness, following the ASTM E384-99 [35] standard, applying a load of 3 N. The CS-ed coatings adhesion to the substrate was measured for three samples each thickness using 3 mm thick low-carbon steel discs as substrate attached to the adhesion dollies, an adapted system of the ASTM C633-13 [26] standard, and using epoxy resin adhesive Ultrabond 100 (HTK, Hamburg, Germany) fully cured at 180 °C for 1 h with traction-adhesive strength of 70 MPa. Fig. 1(a) shows the adhesion testing samples scheme.

2.4. Residual stress

Regarding the CS-ed coatings residual stress measurements, XRD were conducted as a non-destructive method, following ASTM E2860-20 [27] standard. The XRD principle is correlating the lattice spacing, d_0, structure of the feedstock powder and the CS-ed coatings. The lattice spacing variation can be determined from shifts of the diffraction peaks, which are measured by Bragg's law, refering the lattice space with the diffraction angle. The mathematical model to interpret and manipulate the XRD results in this work was $\sin^2\psi$ Ω-tilt mode, described in detail by Luo [28] and Bobzin et al. [29], following the coordinate scheme presented in Fig. 1(c) and varying the angle ψ in the range $0 < \sin^2\psi < 0.8$ with intervals of 0.1. In Fig. 1(c), the "Direction N" vector is normal of the (*hkl*) plane, and the vectors "Incident X-ray", "Diffracted X-ray", and "Direction N" are in the same plane.

For CS-ed Cu, Ti, and 316L coatings the radiation source was Cu Kα, $\lambda = 1.5418$ Å. The lattice strain, ε, was obtained by Eq. (1), where θ_0 is the Bragg angle and $\theta_{\varphi,\psi}$ the measured diffraction angle, following the orientation φ and ψ, Fig. 1(c). The X-ray elastic constants (XEC) were obtained by Eqs. (2) and (3), which consider the material's Poisson's ratio, υ, and Young's modulus, E_{ff}, of the diffracting lattice planes, {*hkl*}, for the different materials evaluated. The literature presents the E_{ff} and υ values for CS-ed Cu, Ti, and 316L coatings used for other residual stress measuring technique [30]: 110 GPa and 0.35 for Cu; 103 GPa and 0.34 for Ti, and 193 GPa and 0.28 for 316L, for E and υ, respectively.

$$\varepsilon_{\varphi,\psi} = \frac{-cot\theta_0 \cdot (2\theta_{\varphi,\psi} - 2\theta_0)}{2} \quad (1)$$

$$s_1^{\{hkl\}} = \frac{-\upsilon}{E_{eff}^{\{hkl\}}} \quad (2)$$

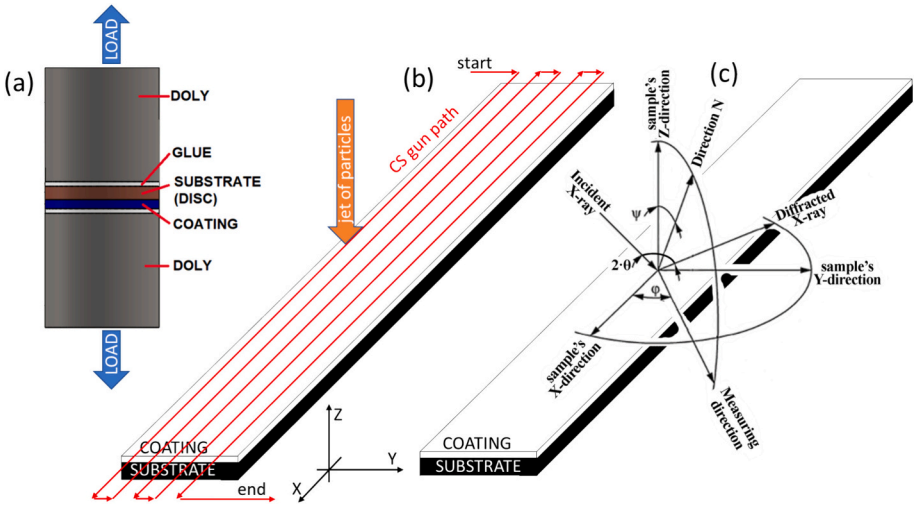

Fig. 1. (a) Adhesion scheme. (b) CS deposition strategy. (c) XRD residual stress measurement scheme, diffraction in N refers to the normal plane to the lattice plane, not to the sample surface.

$$½\cdot s_2^{\{hkl\}} = \frac{1+\upsilon}{E_{eff}^{\{hkl\}}} \tag{3}$$

XEC were: $s_1 = -2.64\ TPa^{-1}$ and $1/2\ s_2 = 10.35\ TPa^{-1}$ for Cu (420); $s_1 = -2.80\ TPa^{-1}$ and $1/2\ s_2 = 11.52\ TPa^{-1}$ for Ti (213); and $s_1 = -1.35\ TPa^{-1}$ and $1/2 \cdot s_2 = 6.18\ TPa^{-1}$ for 316L (420). XEC values are added in Eq. (4) to describe alternatively Eq. (1), considering the theory of elasticity and the triaxial stress state, and that due to the shallow depth of penetration of X-rays at the free surface, stress normal to the surface, *Z*-direction, σ_{zz} is assumed to be insignificant.

$$\begin{aligned}\varepsilon_{\varphi,\psi} = {} & ½\cdot s_2^{\{hkl\}}\cdot[\sigma_\varphi - \sigma_{zz}]\cdot sin^2\psi + ½\cdot s_2^{\{hkl\}}\cdot\tau_\varphi\cdot sin(2\varphi) \\ & + \left(½\cdot s_2^{\{hkl\}} + s_1\right)\cdot\sigma_{zz} + s_1^{\{hkl\}}\cdot\left[\sigma_{xx} + \sigma_{yy}\right]\end{aligned} \tag{4}$$

The normal residual stress on the X- and Y-directions are σ_{xx} and σ_{yy}, respectively. σ_φ is obtained by Eq. (5), as the τ_φ is the shear stress expressed by Eq. (6). To identify the general stress state of the CS-ed coatings, the samples were moved on the axles to scan many positions and φ and ψ angles, keeping the X-ray tube and detector static.

$$\sigma_\varphi = \sigma_{xx}\cdot cos^2\varphi + \sigma_{xy}\cdot sin(2\varphi) + \sigma_{yy}\cdot sin^2\varphi \tag{5}$$

$$\tau_\varphi = \sigma_{xz}\cdot cos\varphi + \sigma_{yz}\cdot sin(\varphi) \tag{6}$$

3. Results and discussions

The experiment results are presented in different sections, starting with the characterizations of the feedstock powders since it is fundamental to know their characteristics before spraying, guaranteeing that they are adequate for the deposition. After the CS deposition, the coatings are characterized, presenting their microstructure, microhardness, DE, adhesion to the substrate, and the evolution of the coating residual stress with the coating thickness for Cu, Ti, and 316L.

3.1. Characterization of feedstock powders

Fig. 2 shows SEM images of the feedstock powders used in this study. It is noticed that some differences in their shape morphology result from the manufacturing process employed for each one. The water-atomized 316L had an irregular morphology, while the gas-atomized Cu and Ti are spherical particles with a few satellite particles attached to the bigger ones. The high spheroidicity observed for Cu and Ti is a result of using an inert atomizing gas and optimized atomizing parameters [31] because changing the atomizer nozzle design and gas flow and pressure alters the spherical shape to a well-rounded one [32], which is similar to the 316L shape seen in Fig. 2.

The particles shape influences the powder flowability, and irregular powders tend to have lower flow rates in free-flowing testing using the Carney funnel; however, for high-pressure CS, the powders are fed under pressure, diminishing the effect of the particle shape on the feeding rate. It happened for 316L, which presented a good flowability, as the spherical Cu and Ti powders. The presence of satellite particles is quite common in gas atomized powders. It is attributed to the fabrication process parameters since the satellites are particles previously solidified that adhere to the bigger particles. The particle concentration in the atomization flow, direction of atomizing gas jets, and design of the atomizing chamber, among others, influence the formation of satellite particles, as presented by Beckers et al. [33].

On the other hand, the irregular shape of water-atomized powders, like the 316L studied in this work, has been attributed to the relatively higher water viscosity than the gases. During the atomization, water impinges on the metal molten flow, and this impact fragments the molten stream in a turbulent manner, leading to irregular shapes. Besides that, the possible creation of vapor enveloping the droplets can lead to non-uniform cooling rates compared to the gas atomizing process, considering this last has a lower thermal conductivity [34].

To corroborate the chemical composition and crystallographic structure, as the lattice spacing d_0 of the feedstock powders used in this study, the content of alloying elements and the identification of phases were carried out by ICP and XRD, respectively. Table 2 shows their chemical composition. Pure Cu and pure Ti had no impurities with content higher than 0.1 wt%, and 316L had a composition in agreement with ASTM A240/A240M [35] standard reference, as expected. The XRD diffractograms are shown in Fig. 3, and only one phase was identified for each powder, Cu, α-Ti, and γ- austenite for 316L powder. The ICDD reference codes are 00–004–0836, 00–005–0682, and 00–047–1417 for Cu, Ti, and 316L, respectively.

Fig. 4 shows the powder size distribution histograms measured by LS for Cu, Ti, and 316L powders. It presents the proper size for CS deposition because particles out of this range do not bond by the adiabatic shear instability (ASI) mechanism, as presented by Mauer et al. [14]. An optimum size range presented by Schmidt et al. [11] for CS effective bonding is between −60 + 10 μm, and the Cu, Ti, and 316L powders used for this work are in this range, as seen in Fig. 4, confirming they are proper for CS deposition.

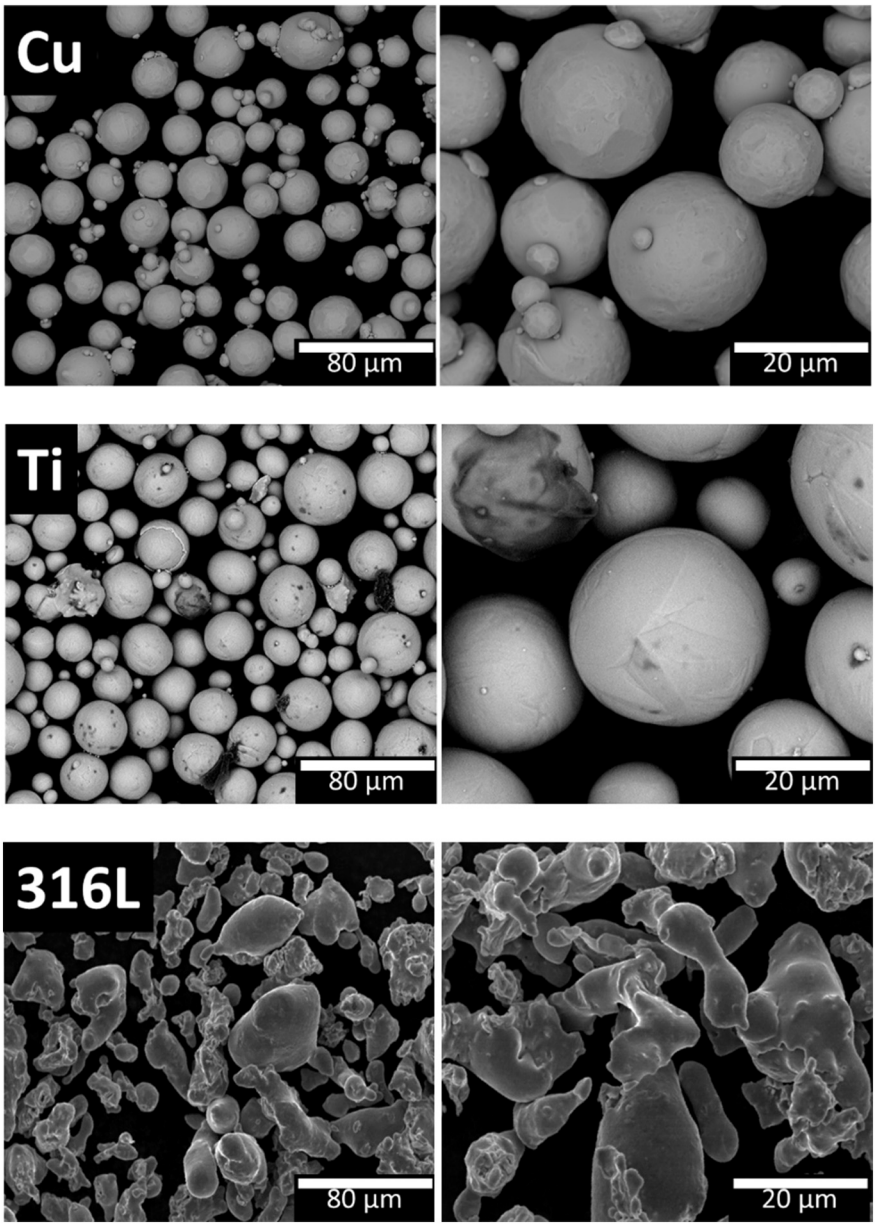

Fig. 2. SEM images of feedstock powders. Magnification: 1000 and 3000×.

Table 2
Feedstock powders chemical composition.

Powder	Nominal Composition [wt%]							
	Cr	Ni	Mo	Mn	Si	Fe	Ti	Cu
Cu								Bal.
Ti							Bal.	
316L	17.6	–	2.7	0.3	0.8	Bal.		

3.2. CS coatings characterization

The CS depositions were performed with 1- and multi-layers. Each material produced a different layer thickness, as presented in Table 3. CS-ed Cu 1-layer resulted in the thinnest coating among the materials studied, 100 ± 12 µm, which can be attributed to a sum of factors: i) its slightly smaller particle size distribution than the other powders, Fig. 4; ii) the higher Cu plasticity than the other powders, which results in more particle deformation and flattening at the impact, Figs. 5–6, and consequently compacting more the material; and iii) a lower DE, Table 3. A peculiarity of Cu and Ti is the severe effect of few oxidizing particles on the CS DE [36]; the feedstock powders used for this deposition were stored under vacuum; however, a minor oxidizing could affect their performance for CS, reducing the DE.

The substrate for all the samples was C-steel with 234 ± 9 $HV_{0.3}$. An Al alloy would be used as substrate, but the adhesion of CS-ed coatings on a thin Al plate would be higher due to the lower Young's modulus and higher plasticity and ductility of Al than C-steel. In this case, an excellent adhesion would also mask the effect of the CS coating thickness on the coating adhesion tendency. Employing a lower stiffness substrate material, such as Al, the coating could bend this substrate more easily, relieving too much the coating residual stress and masking the effect of the coating thickness on this coating property. Comparing the C-steel substrate hardness with the values presented in the Table 3, it is possible to understand the discrepancy in the DE due to the variation of the substrate ductility for 1- and multi-layer coatings. Cu particles were softer than the C-steel substrate, which was prejudicial for ASI and bonding mechanisms of CS-ed Cu coating on a harder substrate because

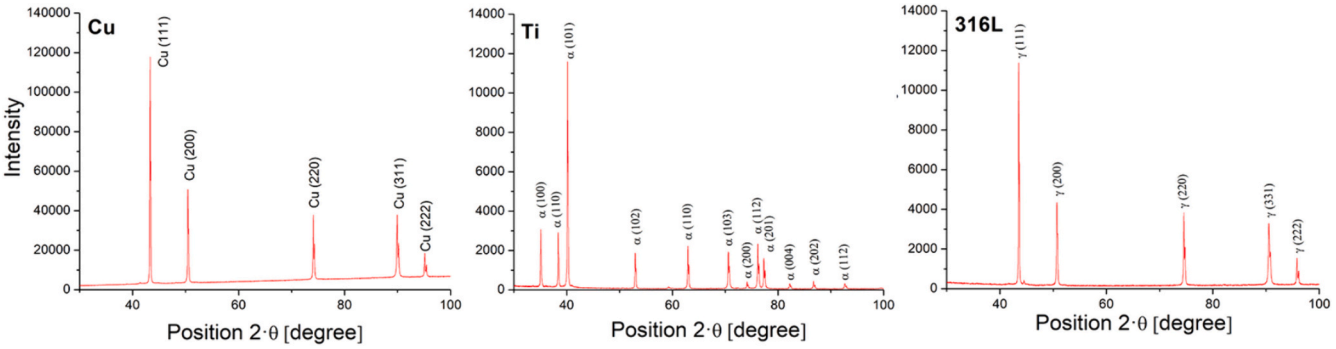

Fig. 3. XRD patterns of the feedstock powders.

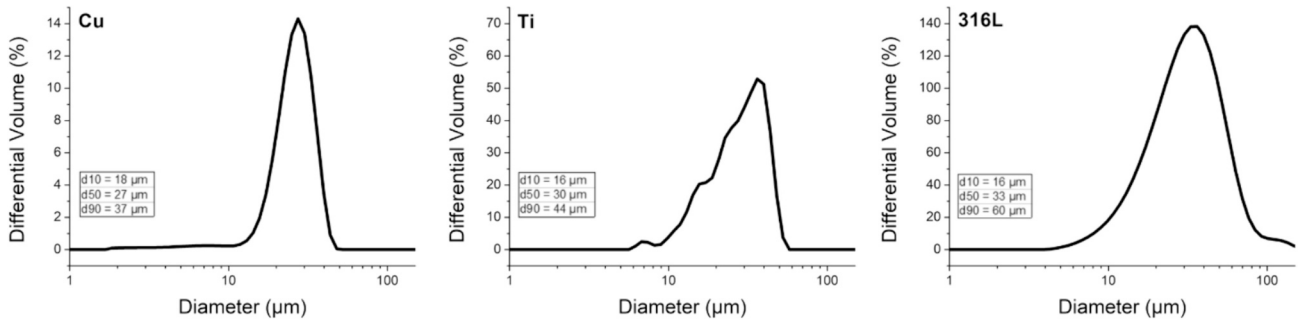

Fig. 4. Particle distribution of the feedstock powders.

Table 3
CS-ed coatings characteristics and properties.

Coating	Layers	Thickness [μm]	Adhesion [MPa]	Porosity [%]	Microhardness [$HV_{0.3}$]	Flattening ratio	DE [%]
Cu	Single (1)	100 ± 12	21 ± 5	<1.0	105 ± 11	2.1 ± 0.5	60
	Multi (10)	1080 ± 8	15 ± 2	<1.0	123 ± 8	2.2 ± 0.4	65
Ti	Single (1)	200 ± 15	23 ± 2	1.7 ± 1.0	224 ± 9	2.1 ± 0.7	89
	Multi (5)	1076 ± 18	19 ± 3	1.5 ± 1.0	214 ± 12	2.2 ± 0.4	95
316L	Single (1)	335 ± 10	29 ± 6	<1.0	280 ± 21	[a]	95
	Multi (3)	912 ± 8	17 ± 5	<1.0	275 ± 15	[a]	91

[a] Not evaluated due to using irregular feedstock powder.

the bonding mechanisms depend on the plastic deformation of the substrate and the particles, and the CS parameters were optimal for the feedstock powder.

However, from the second layer onwards, the CS-ed Cu particles impact onto a Cu layer, which is softer than the previous C-steel, reducing the effect of the harder substrate and increasing the DE from 60 (CS-ed Cu 1-layer) to 65 % (CS-ed Cu multi-layer). A similar DE increase was observed for CS-ed Ti, increasing it from 89 to 97 %. But, for CS-ed 316L, the DE decreased from the 1-layer to the multi-layer coatings. In this case, the close hardness between the CS-ed and the substrate materials helps to improve the DE, because the CS parameters were optimized previously by the CPT team experts to reach the highest DE. However, the hardness effect is superseded by the plasticity changes of the 316L particles when deformed to consolidate the previous layers.

The cold work improves the density of descontinuities, especially in surface/subsurface regions of each particle, with a slight decrease in the DE. The number of multi-layers varied for the different sprayed materials since the target was to produce a 1 mm thick coating. Table 3 shows the number of layers for each material to reach this objective. A thinner individual layer, a lower DE, and a higher number of layers to reach a 1 mm thick coating improves the peening effect on the CS-ed material, densifying and increasing the cold working effect on the microstructure and properties, such as low porosity, high flattening ratio, and high microhardness, among others. Regarding the flattening ratio, numerically no differences were observed from the 1- to multi-layer conditions for CS-ed Cu and Ti, remaining close to 2, which means that the spherical fed powder deforms to a pancake-like particle with the longest dimension twice sized the shortest one. For 316L, the feedstock powder had an irregular shape, and this flattening ratio evaluation was not feasible because there was no evidence of the initial shape of each impacting particle.

The CS depositions produced dense coatings for all conditions studied, employing 1- or multi-layers with porosity below 2 %, as seen in Table 3. Fig. 5 presents microstructures of the materials. The porosity values in Table 3 are the mean values of ten OM of magnification 200× images, and the microstructures seen in Fig. 5 represent this porosity evaluation. It is noticed that the porosity was generated between the low deformed regions of the particles, indicating lower energy at the impact on these regions. One of the reasons for that is the angle of impact since the sprayed particles reach a previously deposited layer composed of deformed particles. This previously deposited material does not result in a homogeneous flat surface for the next layer and the next, and points with deep valleys can result in voids by the incapacity of the particles to deform until the deepest region of these valleys.

Another phenomenon is the particle size distribution because the smallest particles have less volume to deform, and the cold working at

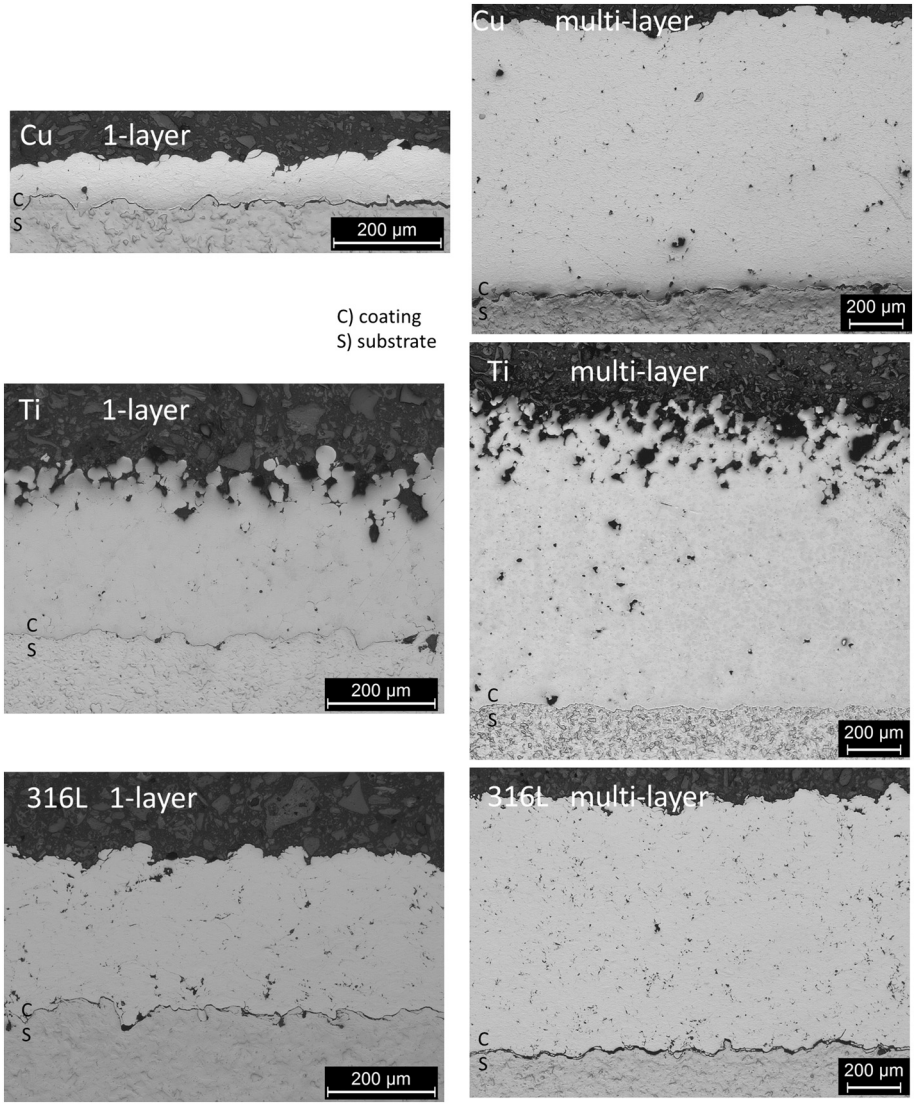

Fig. 5. OM of CS-ed Cu, Ti, and 316L coatings cross-sections. The black areas on the top of images are Bakelite from the mounting.

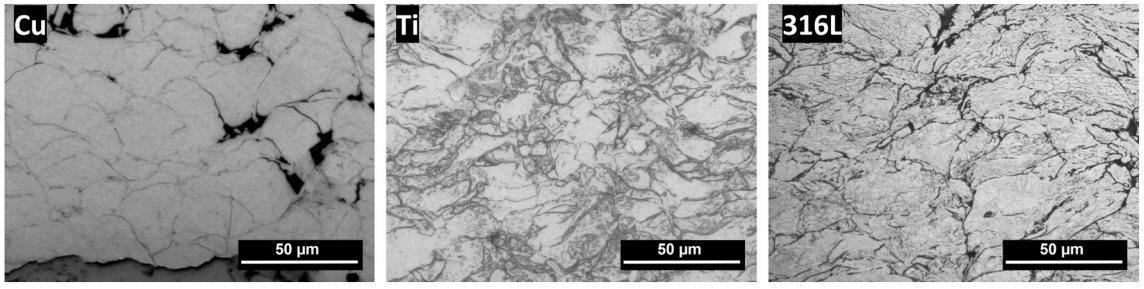

Fig. 6. OM of CS-ed Cu, Ti, and 316L oatings microstructures after etching.

the impact reduces their plasticity, making it difficult to fill these voids. In general, CS produces a controlled porosity level by varying parameters, e.g., higher standoff distance increases the porosity, making it feasible to produce metallic foams [37]. However, CS typically results in coatings with lower porosity than other thermal spraying processes, such as arc-spraying or plasma spraying. The CS coating densification is attributed to the high deformation of particles at the impact onto the substrate, and the next particles keep densifying the previous CS-ed layer by a peening effect, which is effective for ductile materials. This peening phenomenon tends to increase the sprayed material hardness by cold working, which is interpreted by comparing the microhardness of the CS-ed coatings, Table 3, with reference data. CS-ed 316L coating had 280 ± 21 $HV_{0.3}$, and the literature presents 190 HV, for CS-ed 316L annealed [38]; 231 and 166 HV, for selective laser melted 316L as-built and annealed, respectively [39]. The annealing post-processing promotes material recrystallization, where new, strain-free grains grow and replace the cold-worked grains, relieving the material stress with a clear impact on the materials properties, especially hardness reduction [40].

CS-ed Cu and Ti coatings experience the same trend compared to annealed samples.

Table 3 also shows the variation of the adhesion strength of the coatings by increasing their thickness. The 1-layer coatings had higher adhesion values than the multi-layer ones for all studied materials. It was noticed that all the ruptures were adhesive type, i.e., coatings detached completely from the substrate, and no decohesion of particles or delamination between the layers was observed. It is evidence that the cohesion strength is higher than the adhesive strength for the CS-ed Cu, Ti, and 316L coatings studied for 1- and multi-layers.

CS-ed Ti presented a lower adhesion strength reduction, 17 % in mean values; CS-ed Cu decreased the adhesion by 29 % in mean values, from 21 to 15 MPa, and CS 316L by 42 %, from 29 to 17 MPa in mean values. However, considering the standard deviation, the variation is statistically negligible. Fig. 5 shows the interface coating/substrate and it is not observed aligned voids, delamination or detachment, cracks, or incrusted alumina from the grit blasting preparation. This last characteristic indicates that an adequate cleaning process was employed before the CS deposition since few times used alumina was used for grit blasting, following the recommendation presented by Vaz et al. [20] for surface activation for thermal spraying deposition. The effect of the coating thickness on the adhesion is better understood after discussing the residual stress distribution in the coating and, consequently, in the interface coating/substrate. This discussion is presented in the coatings residual stress section.

3.3. CS coatings residual stress

The literature presents the residual stresses classified in three groups: type-I, type-II, and type-III. The first one is homogeneous over multiple grains; type-II are micro-stresses over single grains or in the interface between grains; and type-III are micro-stresses in single grains, but with inhomogeneous over most minor areas such as unit cells [17]. All of the manufacturing processes input or at least alters the residual stress distribution in the material, many of them, including solid-state and thermal spraying process, resulting in tensile residual stress, reducing the working load supported by the mechanical component. However, CS tends to produce coatings with compressive residual stress [9,15,41]. The XRD residual stress measuring technique is particularly effective in measuring type-II micro-stress residual stress in metallic materials due to its ability to analyze the matrial's crystallographic structure. Unlike type-I macro-stresses, which are more uniform and can be measured using traditional stress measurement techniques like strain gauges or Incremental Hole Drilling (IHD), type-II micro-stresses are highly localized and often more challenging to quantify. The XRD quantifies it employing Braggs' law to measure lattice spacing in a crystalline material, and this spacing is affected by external loading imposed to each grain in the material, configuring a type-II residual stress measurement. This lattice spacing deformation is schematically presented in Fig. 7(a-b) for tensile loading; however, for compression loading, the method is the same. Nasiri-Tabrizi [42] presents that a type-II uniform residual stress distribution in the material displaces the diffraction peak from the stress-free position, but a non-uniform residual stress distribution is interpreted by a peak broadening, as presented schematically in Fig. 7 (c). Tensile stress moves the peak to lower 2·θ values, while compressive loading pushes the peak to higher 2·θ values.

A simple view of the CS-ed samples shows this compressive residual stress qualitatively because, during the CS deposition, the steel substrate bent in the negative direction, i.e., the center of the sample gets closer to the CS gun, as seen illustratively in Fig. 8 for the CS-ed 316L sample. This behavior was observed for all the CS-ed samples. The sample bends during the deposition due to force and moment balances in a flat bimetallic plate, considering the couple substrate/coating of this bimetallic material [43]. Other thermal spraying, welding, or cladding processes typically result in positive bending, a clear result of their tensile residual stress. This is an advantage for CS-ed coatings over the cited manufacturing techniques, improving the surface properties to resist mechanical fatigue or corrosion. Considering the bending model presented by Clyne and Gill [30,43] that correlates the residual stress with the bimetallic substrate/coating bending, increasing the CS-ed coating thickness, this volume of material contributes more with the global stress distribution in sample.

More layers are needed to produce a 1 mm thick Cu coating, amplifying the peening stresses, which produces compressive stress in the material by the successive impact under high velocity of the CS

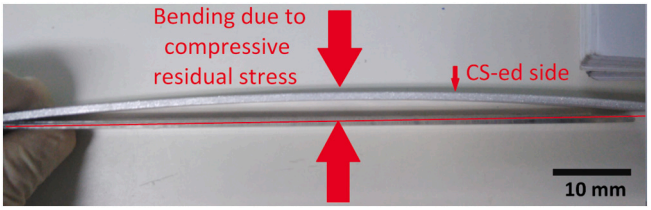

Fig. 8. CS-ed 316L sample bent after the coating deposition.

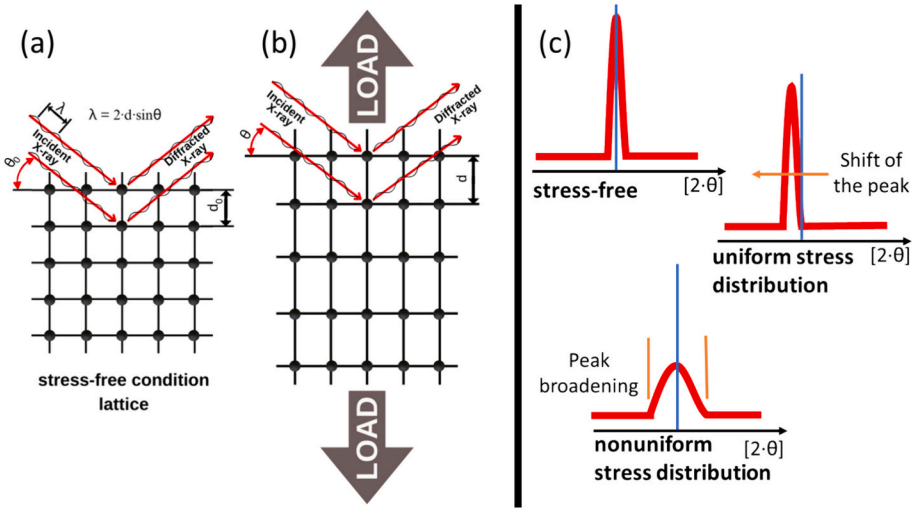

Fig. 7. Scheme of lattice spacing in (a) stress-free and (b) deformed condition, and XRD measuring in a crystalline material due to external to the grain loads. (c) Effects of stress on the XRD diffraction peak.

particles onto the consolidated coating. Other phenomena that result in tensile residual stress for thermal spraying processes is the quenching stresses, related to the rapid cooling of the particles at the impact on the substrate; however, due to the low particle temperature, this mechanism is less important for CS than for the thermally conducted processes, such as plasma spraying or high-velocity oxy-fuel. After the CS deposition, during the cooling time, the different coefficient of thermal expansion (CTE) of the substrate and coating materials is another phenomenon that influences the residual stress, the thermal stresses, which can be a tensile or a compressive value, depending on the CTE mismatch. The substrate, C-steel has CTE 10.8 μm·(m·°C)$^{-1}$, and metallic Cu, Ti, and 316L have CTE 16.7, 8.5, and 16.0 μm·(m·°C)$^{-1}$, respectively. It presents that a mismatch occurs for the bimetallic couple substrate/coating, which is even worse for the CS-ed coating integrity because the interparticular regions act as barriers for the expansion of the material and microcracks can nuclei between the particles or in the interface substrate/coating. However, the thin C-steel plate used as substrate relieved the residual stress by bending, Fig. 8.

This qualitative interpretation of increasing the compressive residual stress in the CS-ed coating by bending the substrate negatively has a positive influence on the adhesion of the coating to the substrate. The substrate bending reduces the tensile stress in the interface; however, employing a stiffer substrate, this tensile stress acts to reduce the adhesion, as seen in Table 3, where all the multi-layer samples had lower adhesion than the 1-layer ones. For CS thick coatings on a stiff substrate, the compressive residual stress acts bending negatively the coating; however, the substrate does not follow this deformation, and an adhesive failure or coating detachment can occur even during the CS deposition or in the cooling down stage. In this case, the failure always starts in the center of the CS-ed coating area, not in the corners of the sample, as happens when the coating has a tensile residual stress.

XRD was used to measure type-II residual stress for CS-ed Cu, Ti, and 316L coatings with 1- and multi-layers, ±1 mm thick, penetrating <20 μm in the material, configuring a near-surface measurement. Fig. 9 shows the residual stress results for the X and Y directions, following the scheme presented in Fig. 1(c). The 2·θ peaks selected were 144.70° for Cu (420), 139.30° for Ti (213), and 146.50° for 316L (420). These peaks were chosen due to their intensity, reducing the time demanded for each data collect. Fig. 9 presents the main stresses in each direction, σ_{φ}, obtained by Eq. (5). As observed qualitatively viewing the bending of the samples after the coating deposition, Fig. 8, XRD revealed numerically the compressive residual stress of the samples.

All the CS samples, 1- and multi-layers, had compressive tension values. A significative evolution was seen for CS-ed Cu samples by increasing the coating thickness, 87 and 57 % in the X and Y directions, respectively, reaching the maximum value among the samples studied, −36.6 ± 1.7 MPa in the X direction with multi-layers. For CS-ed 316L, similar behavior was observed, but with a lower magnitude. For 316L 1-layer and multi-layer, the values were −7.2 ± 4.8 and −15.4 ± 6.4 MPa in the X direction, and −4.5 ± 4.8 and −12.1 ± 3.9 MPa in the Y direction, respectively. However, adding more layers did not significantly alter the residual stress values for CS-ed Ti, remaining close to −15 MPa in all conditions. The slight difference between the residual stress values in X and Y directions is attributed to the sample geometry, which is different in X and Y directions, and to the CS deposition strategy repeated for each layer, which was schematically presented in Fig. 1(a) and has parallels steps in the X direction. This traditional and widely used strategy for thermal spraying processes resulted in planar anisotropy of strength for CS-ed Cu coatings, as presented by Yang et al. [44], due to no uniformity in the particle deformation in the X and Y directions.

4. Conclusions

CS is a solid-state deposition process with great benefits compared to other heat-focused techniques. Understanding the evolution of the coating properties and characteristics with the thickness helps designing new CS coating systems to maximize the coated part performance. This work focused on measuring and evaluating this evolution for CS-ed Cu, Ti, and 316L stainless steel coatings in two conditions: 1-layer and 1 mm thick coating on 2 mm thick C-steel substrate. Several findings can be concluded:

- CS produces Cu, Ti, and 316L coatings with a variety of thicknesses, depending on the number of layers deposited, with high microstructural integrity and absence of defects, such as cracks, detachments, or excessive porosity. Each material has a single-layer thickness value of 100, 200, and 335 μm for Cu, Ti, and 316L, respectively. The following layers, to achieve 1 mm thick coating, maintain a very close thickness value to the first CS-ed layer;
- The coating thickness does not alter the CS-ed Cu, Ti, and 316L coatings microstructural characteristics and properties, maintaining the same low porosity level, high deposition efficienty and flattening ratio, and microhardness with very close values in the different coating thickness samples;
- The CS-ed coating alters the residual stress distribution in the coated substrate. This residual stress is evidenced by its deformation or bending in a negative direction for a thin plate substrate due to the part's low stiffness;
- For a low-stiffness substrate, a low residual stress evolution iss seen by increasing the CS-ed coating thickness. CS-ed Cu and 316L coatings gently increase the compressive residual stress in approx. 17 and 8 MPa, respectively. However, CS-ed Ti coating reduces the compressive residual stress value by approx. 5 MPa.

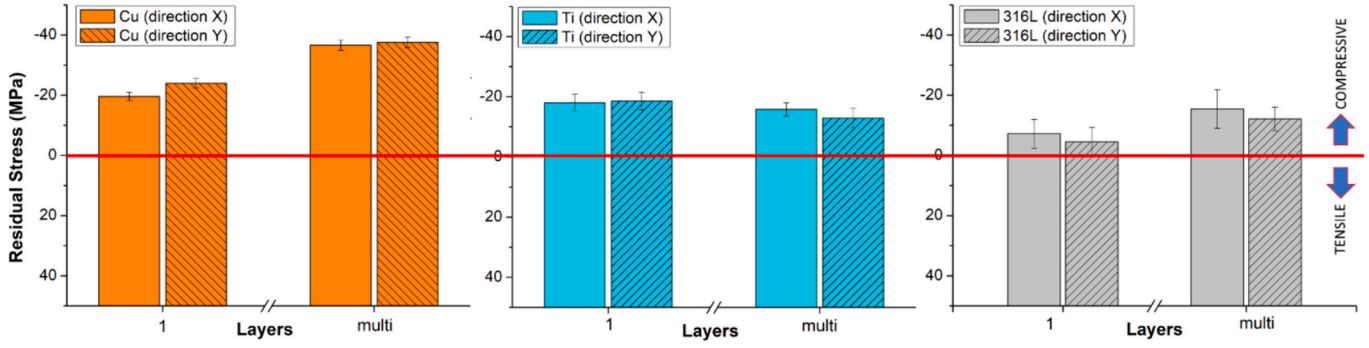

Fig. 9. Residual stress results for CS-ed coatings.

CRediT authorship contribution statement

Rodolpho F. Vaz: Writing – review & editing, Writing – original draft, Methodology, Investigation, Formal analysis, Data curation, Conceptualization. **Andrea Garfias:** Writing – original draft, Investigation. **Vicente Albaladejo:** Writing – review & editing, Writing – original draft, Supervision. **Javier Sanchez:** Supervision, Funding acquisition. **Irene Garcia Cano:** Resources, Project administration, Funding acquisition.

Declaration of competing interest

The authors declare that they have no known competing financial interests or personal relationships that could have appeared to influence the work reported in this paper.

Data availability

Data will be made available on request.

Acknowledgments

Grant PID2020-115508RB-C21 funded by MCIN/AEI/10.13039/501100011033 and, as appropriate, by "ERDF A way of making Europe", by the "European Union" or by the "European Union NextGenerationEU/PRTR". V. Albaladejo is a Serra Hunter Fellow.

References

[1] A. Moridi, S.M. Hassani-Gangaraj, M. Guagliano, M. Dao, Cold spray coating: review of material systems and future perspectives, Surf. Eng. 30 (2014) 369–395, https://doi.org/10.1179/1743294414Y.0000000270.
[2] M. Grujicic, C.L. Zhao, W.S. DeRosset, D. Helfritch, Adiabatic shear instability based mechanism for particles/substrate bonding in the cold-gas dynamic-spray process, Mater. Des. 25 (2004) 681–688, https://doi.org/10.1016/j.matdes.2004.03.008.
[3] M. Hassani-Gangaraj, D. Veysset, V.K. Champagne Jr., K.A. Nelson, Adiabatic shear instability is not necessary for adhesion in cold spray, Acta Mater. 158 (2018) 430–439, https://doi.org/10.1016/j.actamat.2018.07.065.
[4] H. Assadi, F. Gärtner, T. Klassen, H. Kreye, Comment on 'adiabatic shear instability is not necessary for adhesion in cold spray,', Scr. Mater. 162 (2019) 512–514, https://doi.org/10.1016/j.scriptamat.2018.10.036.
[5] T. Hussain, Cold spraying of titanium: a review of bonding mechanisms, microstructure and properties, Key Eng. Mater. 533 (2012) 53–90, https://doi.org/10.4028/www.scientific.net/kem.533.53.
[6] R. Ortiz-Fernandez, B. Jodoin, Hybrid additive manufacturing technology: induction heating cold spray—part I: fundamentals of deposition process, J. Therm. Spray Technol. 29 (2020) 684–699, https://doi.org/10.1007/s11666-020-01005-w.
[7] W. Li, C. Cao, S. Yin, Solid-state cold spraying of Ti and its alloys: a literature review, Prog. Mater. Sci. 110 (2020) 100633, https://doi.org/10.1016/j.pmatsci.2019.100633.
[8] D. Guo, M. Kazasidis, A. Hawkins, N. Fan, Z. Leclerc, D. MacDonald, A. Nastic, R. Nikbakht, R. Ortiz-Fernandez, S. Rahmati, M. Razavipour, P. Richer, S. Yin, R. Lupoi, B. Jodoin, Cold spray: over 30 years of development toward a hot future, J. Therm. Spray Technol. 31 (2022) 866–907, https://doi.org/10.1007/s11666-022-01366-4.
[9] R.F. Vaz, A. Garfias, V. Albaladejo, J. Sanchez, I.G. Cano, A review of advances in cold spray additive manufacturing, Coatings 13 (2023) 267, https://doi.org/10.3390/coatings13020267.
[10] R.F. Vaz, A. Silvello, J. Sanchez, V. Albaladejo, I.G.G. Cano, The influence of the powder characteristics on 316L stainless steel coatings sprayed by cold gas spray, Coatings 11 (2021) 168, https://doi.org/10.3390/coatings11020168.
[11] T. Schmidt, F. Gärtner, H. Assadi, H. Kreye, Development of a generalized parameter window for cold spray deposition, Acta Mater. 54 (2006) 729–742, https://doi.org/10.1016/j.actamat.2005.10.005.
[12] H. Canales, I.G. Cano, S. Dosta, Window of deposition description and prediction of deposition efficiency via machine learning techniques in cold spraying, Surf. Coat. Technol. 401 (2020) 1–10, https://doi.org/10.1016/j.surfcoat.2020.126143.
[13] L. Palodhi, B. Das, H. Singh, Effect of particle size and morphology on critical velocity and deformation behavior in cold spraying, J. Mater. Eng. Perform. 30 (2021) 8276–8288, https://doi.org/10.1007/s11665-021-05997-6.
[14] G. Mauer, R. Singh, K.-H. Rauwald, S. Schrüfer, S. Wilson, R. Vaßen, Diagnostics of cold-sprayed particle velocities approaching critical deposition conditions, J. Therm. Spray Technol. 26 (2017) 1423–1433, https://doi.org/10.1007/s11666-017-0596-8.
[15] M. Ashokkumar, D. Thirumalaikumarasamy, T. Sonar, S. Deepak, P. Vignesh, M. Anbarasu, An overview of cold spray coating in additive manufacturing, component repairing and other engineering applications, J. Mech. Behav. Mater. 31 (2022) 514–534, https://doi.org/10.1515/jmbm-2022-0056.
[16] W. Sun, A.W.-Y. Tan, K. Wu, S. Yin, X. Yang, I. Marinescu, E. Liu, Post-process treatments on supersonic cold sprayed coatings: a review, Coatings 10 (2020) 123, https://doi.org/10.3390/coatings10020123.
[17] M. Hauer, S. Krebs, W. Kroemmer, K.M. Henkel, Correlation of residual stresses and coating properties in arc-sprayed coatings on different substrates for maritime applications, J. Therm. Spray Technol. 29 (2020) 1289–1299, https://doi.org/10.1007/s11666-020-01020-x.
[18] A. Moridi, S.M. Hassani-Gangaraj, S. Vezzú, L. Trško, M. Guagliano, Fatigue behavior of cold spray coatings: the effect of conventional and severe shot peening as pre-/post-treatment, Surf. Coat. Technol. 283 (2015) 247–254, https://doi.org/10.1016/j.surfcoat.2015.10.063.
[19] ASTM, B822-02 - Standard Test Method for Particle Size Distribution of Metal Powders and Related Compounds by Laser Scattering, ASTM International, West Conshohocken, PA, USA, 2002, https://doi.org/10.1520/B0822-20.
[20] R.F. Vaz, A.G.M. Pukasiewicz, G.B. Sucharski, I.B.A.F. Siqueira, S.M.Z. Odake, R.S.C. Paredes, The reuse of alumina for grit blasting preparation of steel surface for thermal spraying, Int. J. Abras. Technol. 10 (2021) 235, https://doi.org/10.1504/IJAT.2021.120261.
[21] R.F. Vaz, H. Canales, J. Sanchez, U. Ocaña, V. Albaladejo, I. Garcia Cano, Metal knitting: a method to control morphology and properties in cold spray additive manufacturing, in: Therm. Spray 2022 Proc. from Int. Therm. Spray Conf, 2022, pp. 614–621, https://doi.org/10.31399/asm.cp.itsc2022p0614.
[22] ASTM, E1920-03 - Standard Guide for Metallographic Preparation of Thermal Sprayed Coatings, ASTM International, West Conshohocken, PA, USA, 2021, https://doi.org/10.1520/E1920-03R21.
[23] ASTM, E3-11 - Standard Guide for Preparation of Metallographic Specimens, ASTM International, West Conshohocken, PA, USA, 2017, https://doi.org/10.1520/E0003-11R17.
[24] ASTM, B487-85 - Standard Test Method for Measurement of Metal and Oxide Coating Thickness by Microscopical Examination of a Cross Section, ASTM International, West Conshohocken, PA, USA, 2002, https://doi.org/10.1520/B0487-20.
[25] ASTM, E2109-01 - Standard Test Methods for Determining Area Percentage Porosity in Thermal Sprayed Coatings, ASTM International, West Conshohocken, PA, USA, 2021, https://doi.org/10.1520/E2109-01R21.
[26] ASTM, C633-13 - Standard Test Method for Adhesion or Cohesion Strength of Thermal Spray Coatings, ASTM International, West Conshohocken, PA, USA, 2021, https://doi.org/10.1520/C0633-13R21.
[27] ASTM, E2860-12 - Standard Test Method for Residual Stress Measurement by X-Ray Diffraction for Bearing Steels, ASTM International, West Conshohocken, PA, USA, 2020, https://doi.org/10.1520/E2860-20.
[28] Q. Luo, A modified X-ray diffraction method to measure residual normal and shear stresses of machined surfaces, Int. J. Adv. Manuf. Technol. 119 (2022) 3595–3606, https://doi.org/10.1007/s00170-021-08645-4.
[29] K. Bobzin, W. Wietheger, M.A. Knoch, A. Schacht, U. Reisgen, R. Sharma, L. Oster, Comparison of residual stress measurements conducted by X-ray stress analysis and incremental hole drilling method, J. Therm. Spray Technol. 29 (2020) 1218–1228, https://doi.org/10.1007/s11666-020-01056-z.
[30] T. Suhonen, T. Varis, S. Dosta, M. Torrell, J.M.M. Guilemany, Residual stress development in cold sprayed Al, Cu and Ti coatings, Acta Mater. 61 (2013) 6329–6337, https://doi.org/10.1016/j.actamat.2013.06.033.
[31] S. Lagutkin, L. Achelis, S. Sheikhaliev, V. Uhlenwinkel, V. Srivastava, Atomization process for metal powder, Mater. Sci. Eng. A 383 (2004) 1–6, https://doi.org/10.1016/j.msea.2004.02.059.
[32] D.M. Goudar, V.C. Srivastava, G.B. Rudrakshi, Effect of atomization parameters on size and morphology of Al-17Si alloy powder produced by free fall atomizer, Eng. J. 21 (2017) 155–168, https://doi.org/10.4186/ej.2017.21.1.155.
[33] D. Beckers, N. Ellendt, U. Fritsching, V. Uhlenwinkel, Impact of process flow conditions on particle morphology in metal powder production via gas atomization, Adv. Powder Technol. 31 (2020) 300–311, https://doi.org/10.1016/j.apt.2019.10.022.
[34] S. Hoeges, A. Zwiren, C. Schade, Additive manufacturing using water atomized steel powders, Met. Powder Rep. 72 (2017) 111–117, https://doi.org/10.1016/j.mprp.2017.01.004.
[35] ASTM, A240/A240M-22a - Standard Specification for Chromium and Chromium-Nickel Stainless Steel Plate, Sheet, and Strip for Pressure Vessels and for General Applications, ASTM International, West Conshohocken, PA, USA, 2022, https://doi.org/10.1520/A0240_A0240M-22A.
[36] C.J. Li, H.T. Wang, Q. Zhang, G.J. Yang, W.Y. Li, H.L. Liao, Influence of spray materials and their surface oxidation on the critical velocity in cold spraying, J. Therm. Spray Technol. 19 (2010) 95–101, https://doi.org/10.1007/s11666-009-9427-x.
[37] F. Rubino, P. Ammendola, A. Astarita, F. Raganati, A. Squillace, A. Viscusi, R. Chirone, L. Carrino, An innovative method to produce metal foam using cold gas dynamic spray process assisted by fluidized bed mixing of precursors, Key Eng. Mater. 651–653 (2015) 913–918, https://doi.org/10.4028/www.scientific.net/KEM.651-653.913.
[38] B. Al-Mangour, P. Vo, R. Mongrain, E. Irissou, S. Yue, Effect of heat treatment on the microstructure and mechanical properties of stainless steel 316L coatings produced by cold spray for biomedical applications, J. Therm. Spray Technol. 23 (2014) 641–652, https://doi.org/10.1007/s11666-013-0053-2.

[39] I. Morozova, C. Kehm, A. Obrosov, Y. Yang, K.U.M. Miah, E. Uludintceva, S. Fritzsche, S. Weiß, V. Michailov, On the heat treatment of selective-laser-melted 316L, J. Mater. Eng. Perform. 32 (2023) 4295–4305, https://doi.org/10.1007/s11665-022-07404-0.
[40] A. Garfias, R. Vaz, V. Albaladejo-Fuentes, J. Sánchez, I.G. Cano, Geometry and microstructure control of remanufactured metallic parts by cold spray additive manufacturing, Materials (Basel) 16 (2023) 4735, https://doi.org/10.3390/ma16134735.
[41] A.G.M. Pukasiewicz, W.R. de Oliveira, R.F. Váz, G.B. de Souza, F.C. Serbena, S. Dosta, I.G. Cano, Influence of the deposition parameters on the tribological behavior of cold gas sprayed FeMnCrSi alloy coatings, Surf. Coat. Technol. 428 (2021) 127888, https://doi.org/10.1016/j.surfcoat.2021.127888.
[42] B. Nasiri-Tabrizi, Thermal treatment effect on structural features of mechano-synthesized fluorapatite-titania nanocomposite: a comparative study, J. Adv. Ceram. 3 (2014) 31–42, https://doi.org/10.1007/s40145-014-0090-4.
[43] T.W. Clyne, S.C. Gill, Residual stresses in thermal spray coatings and their effect on interfacial adhesion: a review of recent work, J. Therm. Spray Technol. 5 (1996) 401–418, https://doi.org/10.1007/BF02645271.
[44] K. Yang, W. Li, X. Yang, Y. Xu, Anisotropic response of cold sprayed copper deposits, Surf. Coat. Technol. 335 (2018) 219–227, https://doi.org/10.1016/j.surfcoat.2017.12.043.